

REPORT DOCUMENTATION PAGE

Form Approved
OMB No. 0704-0188

The public reporting burden for this collection of information is estimated to average 1 hour per response, including the time for reviewing instructions, searching existing data sources, gathering and maintaining the data needed, and completing and reviewing the collection of information. Send comments regarding this burden estimate or any other aspect of this collection of information, including suggestions for reducing the burden, to the Department of Defense, Executive Service Directorate (0704-0188). Respondents should be aware that notwithstanding any other provision of law, no person shall be subject to any penalty for failing to comply with a collection of information if it does not display a currently valid OMB control number.

PLEASE DO NOT RETURN YOUR FORM TO THE ABOVE ORGANIZATION.

1. REPORT DATE (DD-MM-YYYY) 12/05/2011		2. REPORT TYPE Final Technical		3. DATES COVERED (From - To) 03/01/08-05/14/11	
4. TITLE AND SUBTITLE Strain Compatible Oxidation and Corrosion Protection Coatings for Enhanced Thermo-Mechanical Durability of Turbine Airfoils				5a. CONTRACT NUMBER	
				5b. GRANT NUMBER N00014-08-1-0331	
				5c. PROGRAM ELEMENT NUMBER	
6. AUTHOR(S) Tresa M. Pollock				5d. PROJECT NUMBER	
				5e. TASK NUMBER	
				5f. WORK UNIT NUMBER 332	
7. PERFORMING ORGANIZATION NAME(S) AND ADDRESS(ES) The Regents of the University of California, Santa Barbara 3227 Cheadle Hall, 3rd Floor Santa Barbara, CA 93106-2050				8. PERFORMING ORGANIZATION REPORT NUMBER	
9. SPONSORING/MONITORING AGENCY NAME(S) AND ADDRESS(ES) Office of Naval Research 875 North Randolph Street Arlington, VA 22203-1995				10. SPONSOR/MONITOR'S ACRONYM(S) ONR	
				11. SPONSOR/MONITOR'S REPORT NUMBER(S)	
12. DISTRIBUTION/AVAILABILITY STATEMENT "Approved for Public Release; Distribution is Unlimited."					
13. SUPPLEMENTARY NOTES <p style="text-align: center; font-size: 2em; color: purple;">20111223008</p>					
14. ABSTRACT As critical components of advanced aircraft engines, turbine airfoils require coatings for enhancement of oxidation, corrosion and thermal capabilities. Airfoil coatings often constitute a significant fraction of the overall airfoil wall thickness and may therefore strongly influence the overall thermo-mechanical response of the turbine blade. However, to date, coatings have not been designed to enhance the system performance, since the coating-substrate degradation mechanisms under relevant mechanical cycling conditions are not well understood and coating properties are often unknown.					
15. SUBJECT TERMS					
16. SECURITY CLASSIFICATION OF:			17. LIMITATION OF ABSTRACT	18. NUMBER OF PAGES 19	19a. NAME OF RESPONSIBLE PERSON Tresa M. Pollock
a. REPORT	b. ABSTRACT	c. THIS PAGE			19b. TELEPHONE NUMBER (Include area code) (805) 893-3810

**Strain Compatible Oxidation and Corrosion Protection Coatings for Enhanced
Thermo-mechanical Durability of Turbine Airfoils**
Final Report: Grant N00014-08-0331

Technical Objectives

As critical components of advanced aircraft engines, turbine airfoils require coatings for enhancement of oxidation, corrosion and thermal capabilities. Airfoil coatings often constitute a significant fraction of the overall airfoil wall thickness and may therefore strongly influence the overall thermo-mechanical response of the turbine blade. However, to date, coatings have not been designed to enhance the mechanical performance of the system, since the coating-substrate degradation mechanisms under relevant mechanical cycling conditions are not well understood and coating properties are often unknown.

Damage that accumulates in turbine airfoils during service is driven by the superposition of centrifugal and vibratory stresses with airfoil surface compressive stresses that arise due to internal air cooling. Material degradation in this environment is poorly understood due the presence of the multiple material layers (one or more coatings, an interdiffusion zone and a superalloy substrate) that can crack, deform by creep and oxidize simultaneously. Due to complexity of the degradation process, improvements in airfoil durability are unlikely to be achieved without models of the degradation process that contain the essential materials and mechanics details. Thus the technical objectives of this research effort are threefold: (1) to establish a fundamental, mechanistic understanding of the degradation processes that occur in superalloy components with coatings during thermo-mechanical cycling; (2) to develop models for damage growth under cyclic conditions that can guide development of strain compatible coating systems and (3) to transition models to Navy turbine manufacturers for their use in alloy coating design and lifing.

Technical Approach

The project is a combined experimental and modeling effort. To study crack advance mechanisms, experimental thermomechanical cycling experiments have been conducted on single crystal substrates with a variety of coatings. Strain-controlled fatigue cycling experiments with compressive holds have been conducted in the temperature range of 982°C – 1080°C. Since creep occurs during these compressive holds, the high temperature properties of the coating as well as the substrate are key elements of the degradation process. The cycling experiments have been designed and conducted in collaboration with GE Aviation, since this cycle is a key

materials/coatings design and selection metric [1]. The primary single crystal substrate is René N5, a commercial single crystal alloy that is present in most GE commercial and military engines. Additional collaborations with the National Institute for Materials Science (NIMS) in Tsukuba, Japan have also permitted exploration of a new class of coatings

Progress

Mechanisms of crack initiation and advance have been studied in detail in René N5 and in a Ta-modified version of this single crystal. Alloy compositions are listed in Table 1. Vapor phase aluminide coated fatigue samples with a 5mm gage diameter and 19mm gage length were fabricated for testing. Strain-controlled fatigue cycling experiments with 120s. compressive holds have been conducted in the temperature range of 982°C – 1080°C.

Table 1 – Compositions of the Experimental Single Crystal Superalloys (wt%)

Alloy	Co	Cr	Mo	W	Ta	Al	Re	Hf	Ni
René N5	7.5	7.0	1.5	5.0	6.5	6.2	3.0	0.15	Bal
High Ta	7.6	7.0	1.5	5.1	9.3	5.6	3.0	0.14	Bal

The **Sustained Peak Low Cycle Fatigue** test is referred to as **SPLCF**. During the compressive hold, creep deformation occurs, resulting in tension upon unloading, Fig 1. Due to creep, tensile stresses develop during unloading. This occurs early in life, typically within the first few cycles, as shown

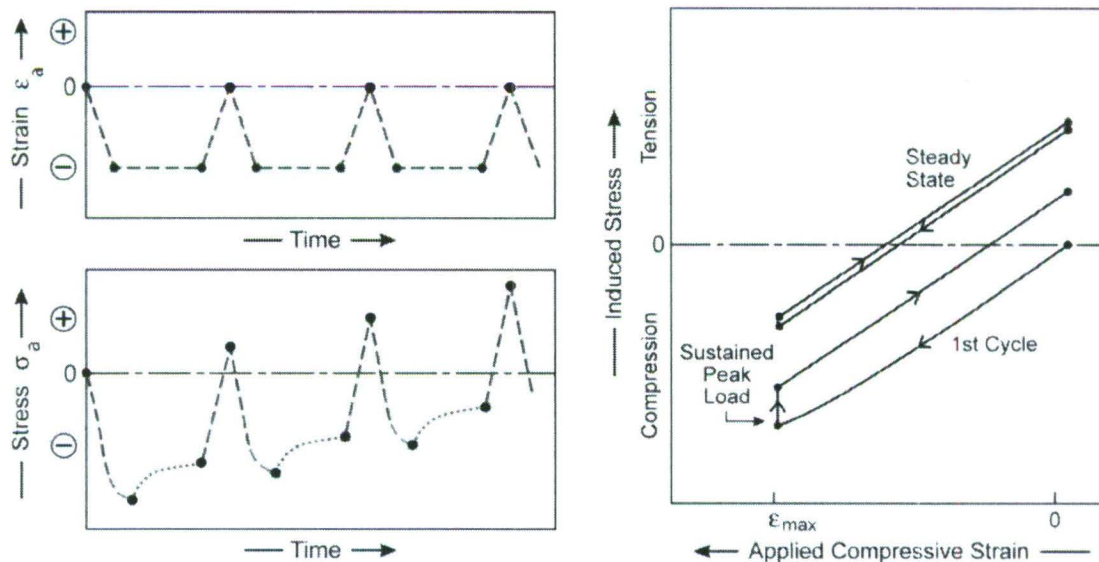


Figure 1 - Schematics of the applied straining conditions associated with sustained peak load cyclic fatigue. (a) The compressive strains imposed and trends in the stresses induced as cycling proceeds. (b) The stress/strain loops and their evolution with cycling.

for René N5 at 1093°C, Fig. 2. If coating cracks are present, the tensile unloading results in crack opening and permits an alumina layer to form along the crack surfaces, Fig. 3. The alumina layer is analogous to the thermally grown oxide (TGO) that has been studied extensively in prior coating oxidation studies (without the presence of cracks); key insights from this prior research [2 - 10] are considered in the modeling efforts within this program, as described in detail below.

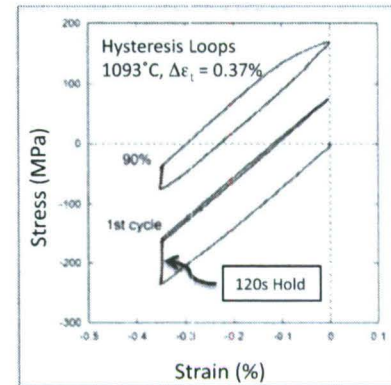
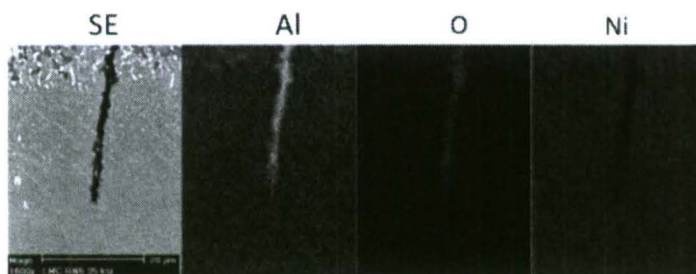


Figure 2-Hysteresis loops for René N5 at 1093°C

Experimental Observations

SPLCF cycling of samples to failure as well as experiments interrupted at various fractions of the average failure life have been conducted on René N5. These experiments have revealed four successive stages of the failure process (Figs. 4 and 5): crack extension from the surface through the



René N5 / 982°C / 2 min Compressive Hold

Figure 3- SEM secondary image and corresponding X-ray maps showing alumina in the crack tip after SPLCF testing.

(I) bond coat (BC), (II) interdiffusion zone (IDZ), (III) superalloy substrate and (IV) long crack growth. For the alloys and cyclic conditions studied here, a large fraction of the total cyclic life is spent in crack propagation through the vapor phase aluminide bond coat and associated interdiffusion zone. An example of this is shown in Fig. 6, where samples of René N5 interrupted after 1000, 2000, 4000, 6000, and 8000 cycles (approximately 10%, 20%, 40%, 60% and 80% of life, respectively) at 1093°C and $\Delta\epsilon_t = 0.35\%$ are sectioned longitudinally. Cracks do not penetrate beyond the interdiffusion zone until approximately 80% of the life is consumed by cycling. Cracks form on a plane normal to the tensile stress and remain in this orientation through the first three stages of cycling. Eventually in Stage IV, the crack length exceeds the long crack cyclic threshold and macroscopic crack growth occurs along an inclined plane in a mixed-mode manner (Fig. 5). This Stage IV long crack growth is the final failure stage and only occurs very late in life. For this reason, finite element modeling has focused on the development of cracking in the first three stages. Crack depths and approximate crack growth rates have been measured for each of the first three stages, Fig. 7.

(I) bond coat (BC), (II) interdiffusion zone (IDZ), (III) superalloy substrate and (IV) long crack growth. For the alloys and cyclic conditions studied here, a large fraction of the total cyclic life is spent in crack propagation through the vapor phase aluminide bond coat and associated

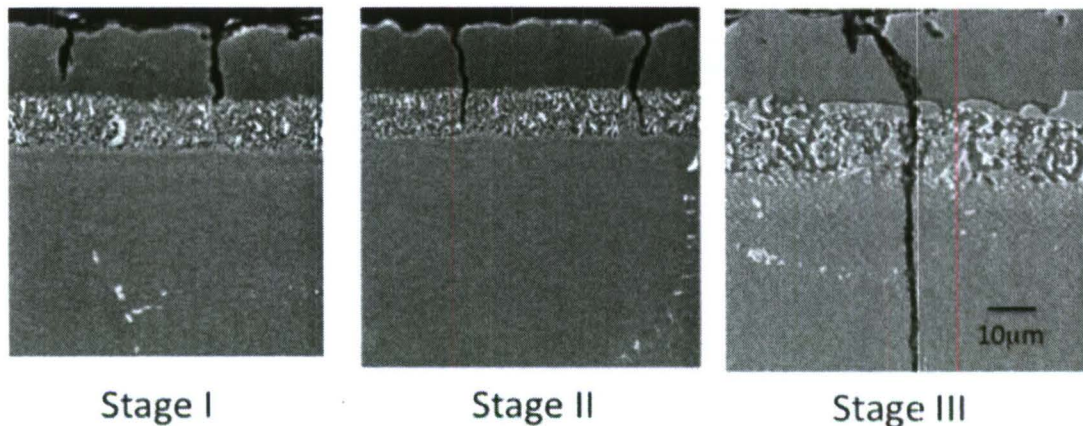


Figure 4-The first three stages of crack progression with cracking in the bond coat (Stage I), interdiffusion zone (Stage II) and superalloy substrate (Stage III).

Comparative SPLCF tests were also conducted at 982°C over a range of alternating pseudo stress on the above two alloys, each grown by both conventional Bridgman and Liquid Metal Cooled (LMC) solidification processes [11, 12]. Average primary dendrite arm spacings for the Bridgman and LMC materials were 340µm and 157µm, respectively. Both alloys were given a platinum aluminide coating. The addition of Ta and the use of the LMC process were both expected to improve creep

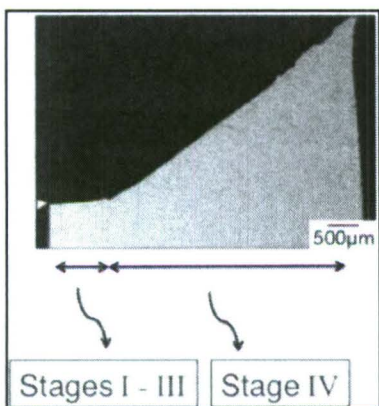


Figure 5-Longitudinal section through a SPLCF sample showing the four stages of failure, with an inclined crack causing final failure in Stage IV.

resistance [11 - 13], thereby influencing the behavior of the substrates under compressive holds. The creep properties at 980°C at stresses of 276 and 414 MPa were investigated (Fig. 8). The René N5 grown by the conventional Bridgman process exhibited the shortest rupture life and the Bridgman and LMC high Ta materials exhibited a rupture life that was approximately 1.6 - 1.8X longer at both stress levels. Under these creep testing conditions, the Ta addition was more effective for improving creep

life, compared to the higher gradient (lower dendrite arm spacing) LMC process. These four material variants were also subjected to SPLCF cycling at 982°C for alternating pseudostresses varying from 227 MPa - 414 MPa (33 ksi - 60 ksi). As shown in Fig. 9, there was a similar degree of variation in SPLCF cycles to failure as observed in creep rupture life. However, a greater number of samples would be need to be tested to determine if there are statistically significant correlations between SPLCF life and creep rupture life. The progression of

cracking was similar to that shown in Figs. 3-6, with the only notable difference being a gamma layer surrounding the crack tip in the high Ta alloy, Fig. 10.

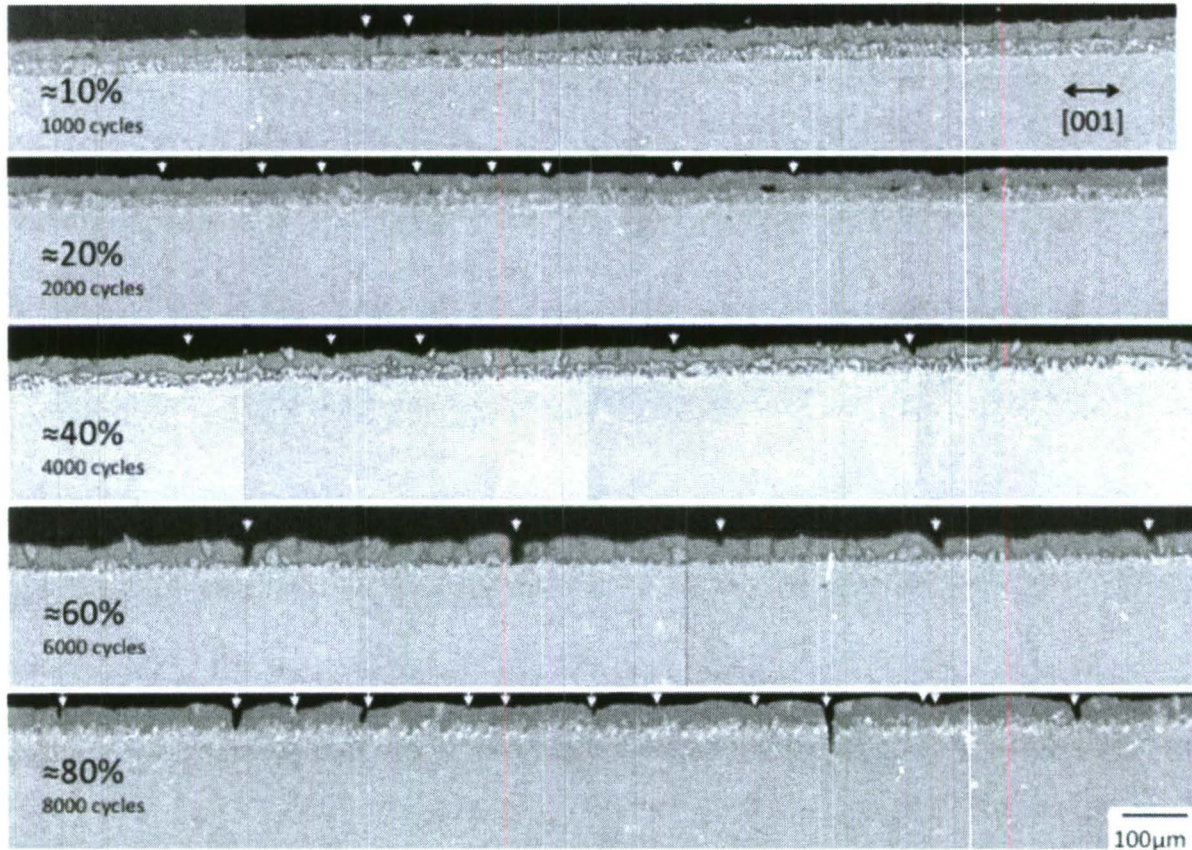


Figure 6-Crack progression as a function of cyclic life for René N5 tested at 1093°C and $\Delta\epsilon_t = 0.35\%$. Compression axis is horizontal.

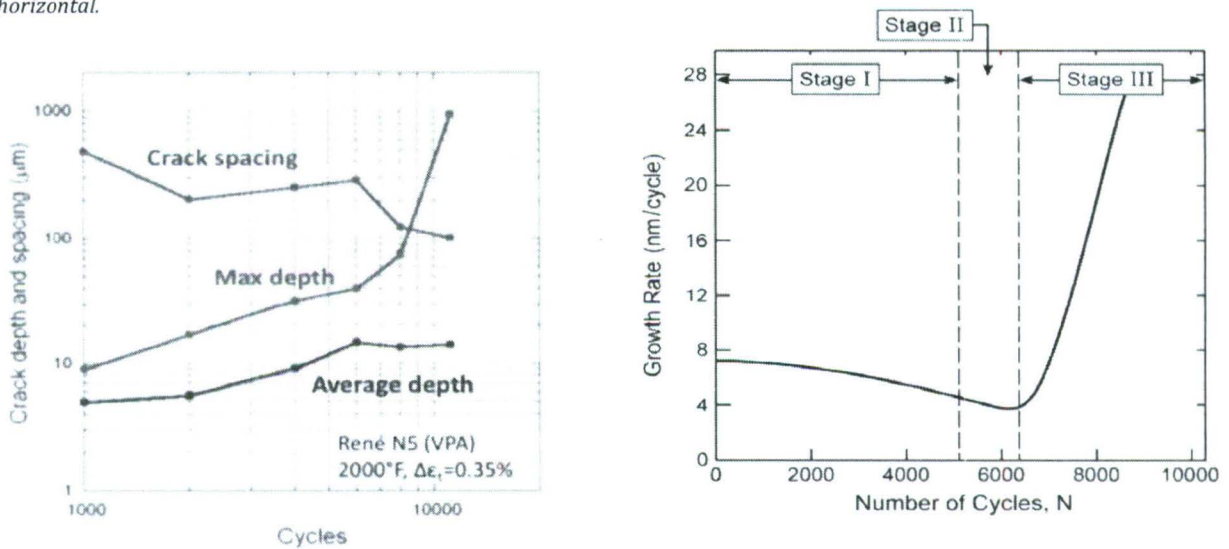


Figure 7-Evolution of crack spacing and depth and average crack growth rate during SPLCF cycling of René N5 at 1093°C.

Finite Element Modeling of the SPLCF Mechanism

A comprehensive finite element modeling effort has been undertaken to elucidate the properties of the coating, interdiffusion zone, thermally grown oxide (TGO) and superalloy substrate that most

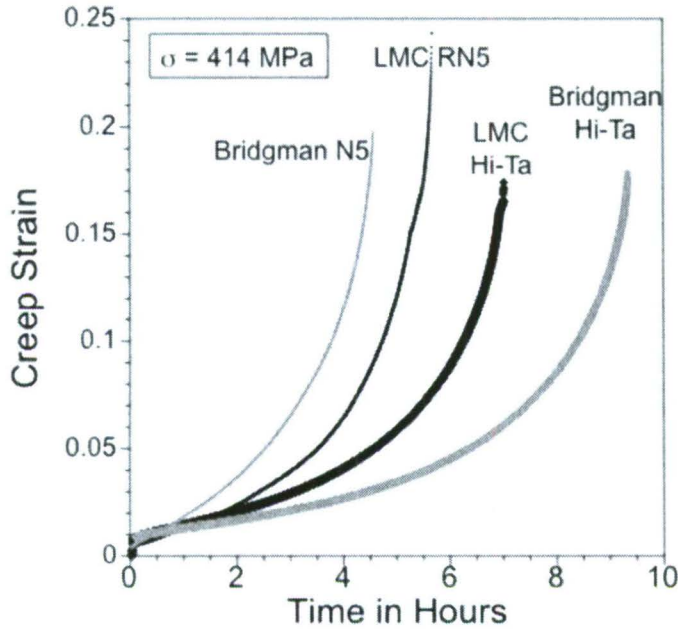


Figure 8-Creep properties of Bridgman and LMC single crystal experimental materials at 982°C.

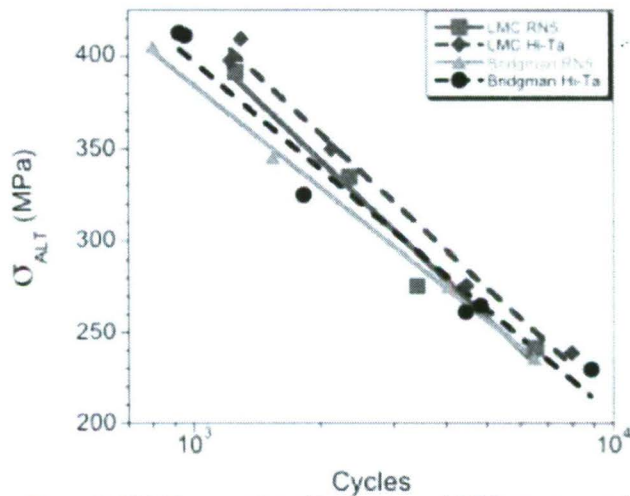


Figure 9- SPLCF properties of Bridgman and LMC experimental materials coated with platinum aluminate and tested at 982°C.

strongly influence the failure process. Different meshes were developed to represent cracks present within the first three different stages of SPLCF. Schematic finite element meshes and a detailed mesh for a Stage III are shown in Figs. 11 and 12.

The model is unique in that it embodies the same mechanics and phenomena previously used to successfully predict rumpling of the thermally-grown oxide (TGO) on bond coats [2-10]. Oxidation of the bond coat occurs by the

formation of polycrystalline, columnar $\alpha - Al_2O_3$. While most of the new oxide forms at the interface with the bond coat by inward diffusion of oxygen, an outward counter-flux of Al causes some new $\alpha - Al_2O_3$ to form along the transverse grain boundaries, as well as at ridges along the surface [2, 3]. The alumina formed on the grain boundaries must be accommodated by

lateral straining of the neighboring grains, at a strain-rate $\dot{\epsilon}_{growth}$ [4 - 6].

The $\alpha - Al_2O_3$ responds by creep, at strain-rate, $\dot{\epsilon}_{creep}$ causing a compressive growth stress, σ_{growth} [4, 5]. The magnitude of this stress has been measured *in situ* for the TGO on several different bond coats. It is of order, $\sigma_{growth} \approx -300 MPa$ [8], consistent with deformation mechanisms for

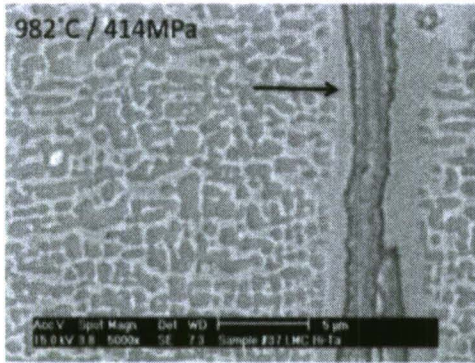


Figure 10-Soft gamma layer surrounding the oxide-filled crack tip in high Ta alloy following SPLCF.

during SPLCF cycling. At the temperatures of interest, the bond coat and superalloy are much softer than the oxide, so the growth stresses have the potential to drive plastic deformation processes in these sub-layers. High temperature properties have been measured in both the

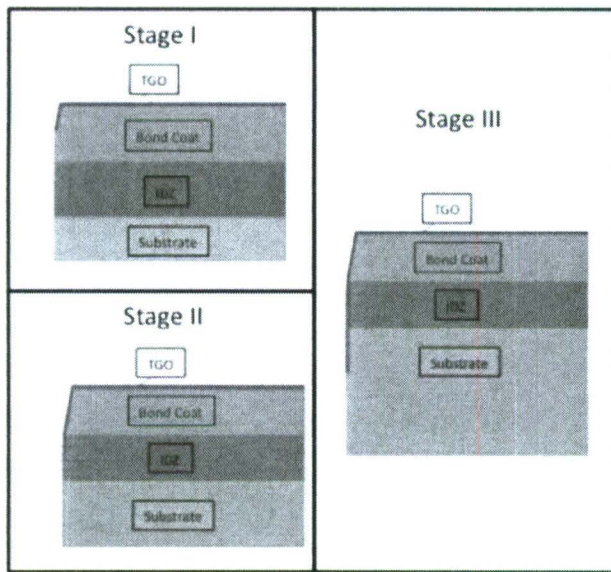


Figure 11-Schematic finite element meshes of the first three stages of the SPLCF process.

NiAl bond coat and the superalloy substrate [17] (Table 3).

The fatigue model proceeds from the rumpling model without any additional physics or mechanics, in accordance with the same numerical implementation. Namely, to capture the lateral straining in the TGO, in the model, $\dot{\epsilon}_{growth}$ is imposed during those stages of the strain cycle when the crack is

$\alpha - Al_2O_3$ and with stress relaxation rates measured in a typical TGO [14]. When the surface is non-planar, the stress σ_{growth} exerts a downward pressure on the bond coat, causing it to creep [8, 15], and motivating the development of crack-like features [10].

In the SPLCF problem, the oxides are forming on the sample surface as well as crack surfaces; it is assumed that these stresses are also present in the oxide formed

substrate [13] and the bond coat [16]. Steady-state creep can be adequately represented by power law behavior of the form: $\dot{\epsilon}_s \approx \dot{\epsilon}_0(\sigma / \sigma_0)^n$, where σ is the local Mises stress, σ_0 is a reference stress, $\dot{\epsilon}_0$ a reference strain rate, and n the creep exponent. Values for these parameters representative of the substrate, TGO and bond coat at 1090°C are summarized in Table 2. The creep properties of alloys with compositions similar to those in the

interdiffusion zone have also been measured. They are intermediate to the β -

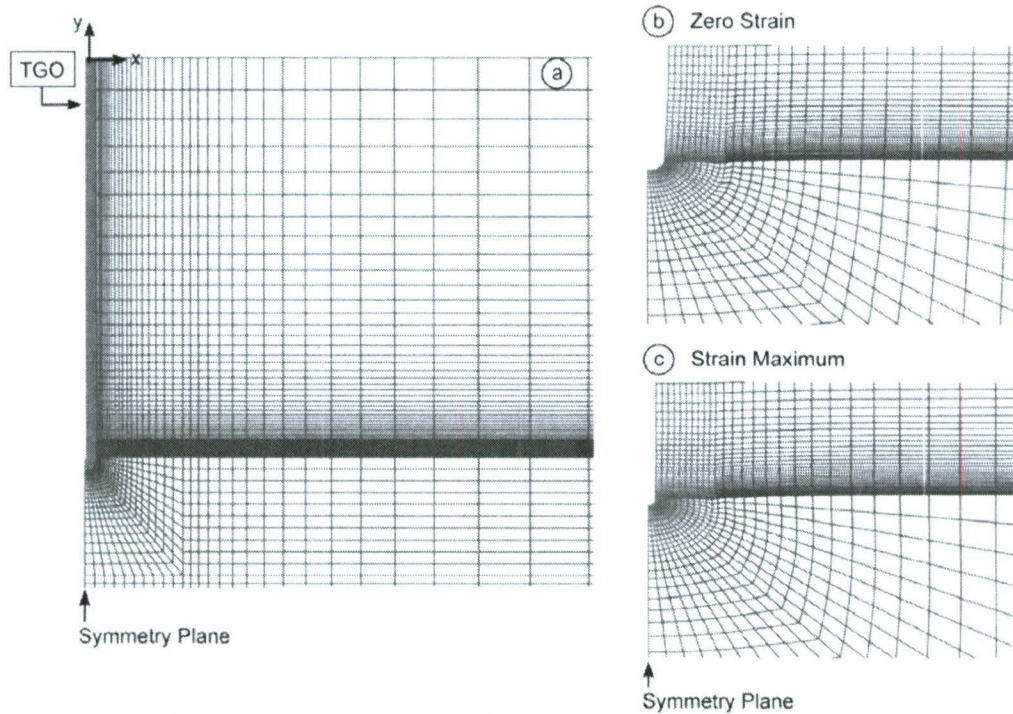


Figure 12- The finite element mesh used for the numerical simulations. Also shown are the configurations when the applied strain is a maximum (crack closed) and when the strain is zero (crack open).

Table 2. Constituent material properties at 1090°C

	Yield Strength σ_y (MPa)	Young's Modulus E (GPa)	Strain Hardening Exponent N	Strain Rate Coefficient $\epsilon_0 (s^{-1})$	Strain Rate Exponent n	Creep Reference Stress σ_0 (MPa)
TGO	300	400	-	-	-	-
Substrate	50-200	74	10	4×10^{-9}	10	100
Bond coat	10-40	74	10	-	-	-

Table 3. Creep strengths of the substrate and coating layers

Composition	Approx Creep Strength @1090C for Creep Rate = $10^{-8}/s$ (MPa)	Reference
René N5 (Substrate)	110	13
Ni-6.3Al-15.1Pt-2Cr-2.9Re-5.6Ta (wt%) - (Interdiffusion Zone)	60	16
B2 (Pt,Ni)Al (Bond Coat)	20	17

open. It is imposed at a uniform rate governed by the TGO thickness. This strain-rate causes creep of the TGO, replicated by ensuring that the Mises stress never exceeds the growth stress, $\sigma_{eq} \leq \sigma_{growth}$. The ensuing response of the TGO is governed by the creep deformation of the surrounding material (bond coat, IDZ or substrate). Namely, creep deformation occurring around the tip accommodates elongation of the TGO, leading to a crack extension per cycle. The five parameters affecting the fatigue crack growth rate are thus: the TGO growth stress, σ_{growth} , the lateral strain-rate experienced by the TGO as it grows, $\dot{\epsilon}_{growth}$, the TGO thickness, h_{TGO} , the creep characteristics of the surrounding material, $\dot{\epsilon}_{sub} \approx \dot{\epsilon}_0(\sigma / \sigma_0)^n$, and the crack length, a . The phenomenon is most readily visualized for Stage III crack extension in the substrate (but equally applicable to V-cracks in the bond coat and IDZ, as described later). Specifically, as the tension becomes substantial upon unloading, the crack opens and the TGO elongates causing outward creep flow of the substrate around its frontal zone to accommodate extension of the crack. Recall that the crack opening upon unloading is a direct consequence of the bulk creep deformation during the

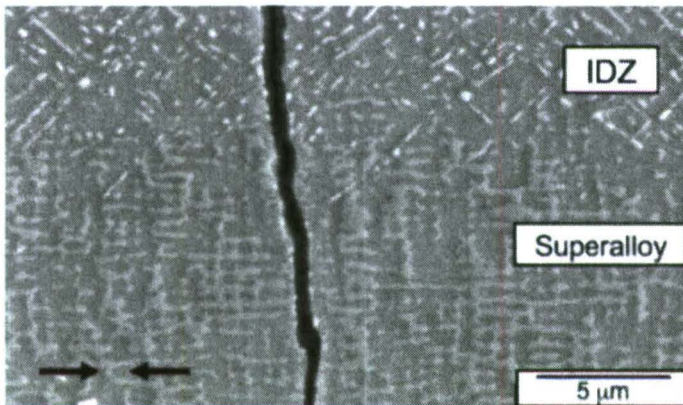


Figure 13 -René N5 sample with a crack extending through the interdiffusion zone (IDZ) into the superalloy substrate following fatigue loading with a compressive hold in the direction indicated by the arrows.

compressive hold, which relaxes the compressive stress. Indeed, direct evidence of uniform compressive creep throughout the sample is provided by the evolution of the precipitate morphology, to plates aligned parallel to the compression axis, Fig. 13. Note also the uniform thickness of the oxide along the crack face, at approximately 6 μm in thickness.

The principal features of the crack growth process can be elucidated with a plasticity model for the substrate and bond coat (with power law hardening) and by invoking the reference stress method to convert to power law creep [18]. This correspondence has been demonstrated for rumpling [5, 15]. The viability is demonstrated below by comparing representative results based on plasticity and creep. Thereafter, for computational efficiency, trends are presented using the plasticity version. The FE code ABAQUS standard is implemented in plane strain, with the meshes depicted in Fig. 11 and 12. The model parameters are those presented in Table 2. For the plasticity analogue, the yield strength for the substrate and the strain hardening exponents are given in Table 2.

Initial results are presented for Stage III growth, where the crack has just penetrated into the superalloy substrate. In the model, a transverse cyclic displacement is imposed in the x-direction, at the outer boundaries, consistent with a compressive strain cycling between 0 and 0.4% (Fig. 2). The oxide and attached layers are free to displace in the y-direction, upward as well as downward into the substrate. The TGO lateral strain is imposed at constant rate, while the crack is open. This is achieved within ABAQUS by imposing an in-plane stress-free strain-rate (similar conceptually to the way thermal expansion and phase changes are addressed). The lateral strain-rate range, $0 \leq \dot{\epsilon}_{growth} \leq 0.05\% / cycle$ has been chosen because of its relevance to the prediction of rumpling rates [5, 15]. Throughout, the growth stress is retained at, $\sigma_{growth} \approx -300 MPa$ [8], and the TGO thickness fixed at the experimentally measured value, $h_{TGO} \approx 3 \mu m$. The yield strength of the substrate is $\sigma_y^{sub} = 100 MPa$, and strain hardening exponent, $N = 10$ (Table 2). Calculations are for 20 cycles with initial crack length, $a_0 = 100 \mu m$ with the extension, Δa , is small relative to a_0 .

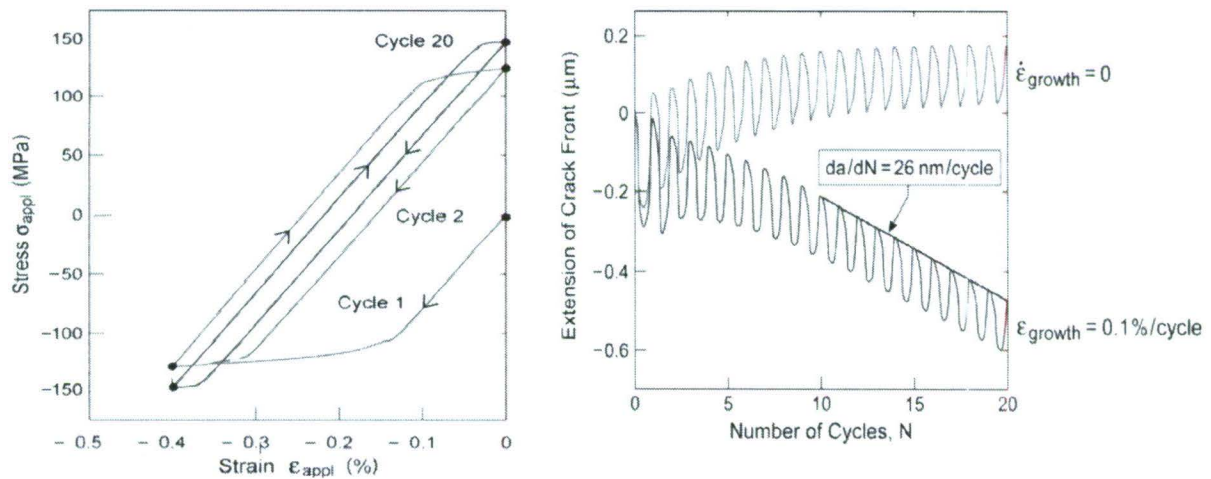


Figure 14- The hysteresis loops calculated using the plasticity model (left), Calculations of the change in crack length in stage III for a representative TGO elongation rate, $\epsilon_{growth} = 0.1\% / cycle$, as well as for $\dot{\epsilon}_{growth} = 0$, contrasting the two situations (right).

The stresses induced at the boundaries during 20 cycles during Stage III growth are presented on Fig. 14. After a few cycles, steady-state is reached and a hysteresis loop having width, $\Delta\epsilon_{hyst} = 0.05\%$ is observed. The cycle-by-cycle extension of the crack front reveals that, after a few cycles, the extension per cycle is invariant and (for this case), at $da/dN = 40 \text{ nm/cycle}$, quite similar to that ascertained experimentally in Stage III, Fig 7, which was $da/dN = 28 \text{ nm/cycle}$ for the corresponding crack length. The corresponding behavior absent a lateral strain rate, $\dot{\epsilon}_{growth} = 0$ (Fig. 14) affirms that continuous fatigue crack growth is linked directly to TGO formation.

Diagnosis of the stresses, strains and displacement during one cycle elucidates the phenomena governing crack extension (Fig. 15). The assessment starts with the crack closed, when the imposed strain is at its maximum. Upon reducing the applied strain, the Poisson effect requires that the substrate retract along the crack plane, causing the TGO to develop in-plane compression (Fig. 16). Addition of the growth strain introduces further in-plane compression, causing the stress in the TGO attains its maximum of -300 MPa. Close to the front, Fig. 15, the transverse compression in the TGO is larger, $\sigma^{tgo} = -600$ MPa because of the triaxiality. The corresponding stress in the substrate is also compressive, but smaller, $\sigma_{xx}^{sub} \approx -120$ MPa. The plastic strain field has features representative of those around cracks, with the largest strains occurring within contours inclined at 30-40° to the crack plane, Fig. 17. In [001] fcc single crystals, this inclination coincides with the

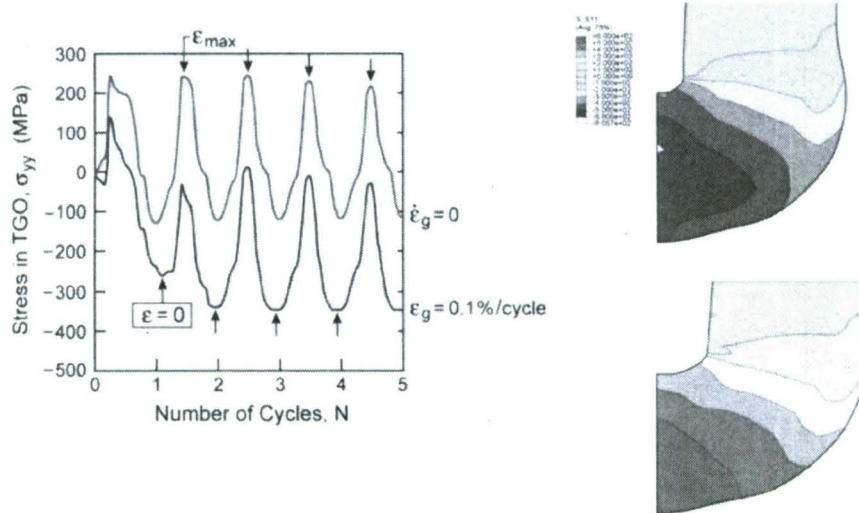


Figure 15 - The stresses induced in the TGO during a strain cycle. (a, left) The in-plane stresses with and without a growth strain. (b, right) The concentrated σ_{xx} stresses ahead of the crack when closed and open.

orientation of the octahedral slip planes to the crack front, indicative of localized slip along these planes during fatigue [19, 20]. These planes are ultimately the direction along which the cracks propagate in Stage IV, when the

mixed-mode cyclic stress intensity becomes sufficiently large [20, 21]. Upon re-loading, the substrate lengthens along the crack plane, causing the TGO to develop in-plane tension, though the growth strain counteracts this tension ϵ_g such that the net in-plane stress in the TGO remains compressive (Fig. 16). This distinction in stress state, with and without a growth strain, has important implications for fatigue, as elaborated in Fig. 16. Each time the crack is open, elements in the substrate ahead of the crack develop incremental plastic stretch normal to the crack with a corresponding orthogonal retraction. These effects happen because the state of in-plane compression (figure 14), enables $\dot{\epsilon}_{growth}$ to elongate the TGO, by "pushing" it into the substrate and

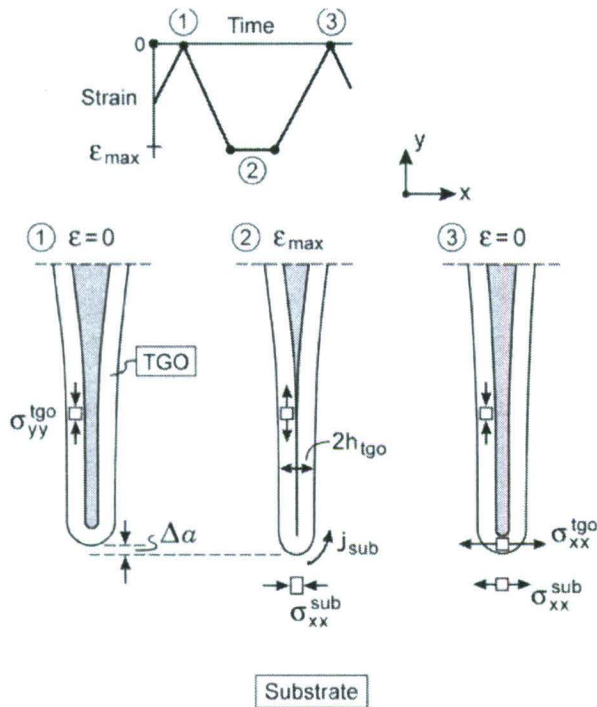


Figure 17- A schematic indicating the stresses induced and the matrix mass flux governing the fatigue mechanism during one strain cycle.

stress/strain responses ascertained over 50 cycles, with 1 h hold for each, are presented in Figs. 17 and 18. Note the similarity between these predictions and the measurements (Fig. 7) in the sense that the tension at zero strain increases systematically as cycling proceeds. A substantial shift in the

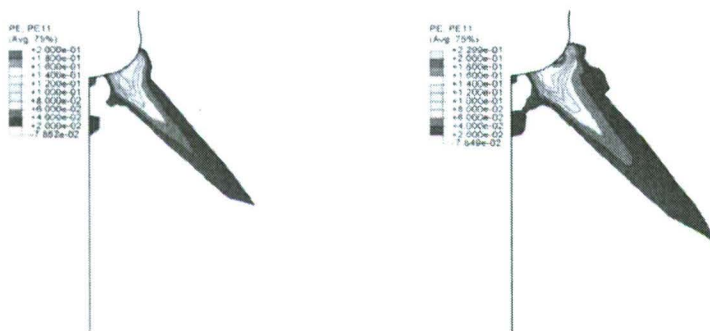


Figure 16- Contours of plastic strain in the substrate; (a, left) at maximum applied strain and (b, right) at zero applied strain.

stress at zero strain occurs after the first cycle, especially at the higher strain rate coefficient. After a few cycles, the hysteresis loop width becomes quite narrow (albeit larger for larger $\dot{\epsilon}_0$), but large enough to cause the stress to systematically shift with each additional cycle. The hysteresis is now caused entirely by stress relaxation at the strain maximum. The cycle-by-cycle crack extension predicted by the model is presented on Fig. 18. Note that, again, there is no fatigue when $\dot{\epsilon}_{growth} = 0$ and that the extension rates are similar to those for the

accommodating its displacement through lateral plastic flow, out from the crack front. Fig. 16 illustrates this series of events and establishes the influence of $\dot{\epsilon}_{growth}$ and TGO elongation as the fundamental basis for fatigue.

To validate the plasticity approach, a creep version of the model was also formulated. In this version, the substrate creep law is used with two different strain-rate coefficients ($\dot{\epsilon}_0 = 4 \times 10^{-8}$ & $4 \times 10^{-9} / s$) that encompass the measurements for the substrate (Table 2). The time for imposing the strain, t_{strain} , has been

chosen to enable non-linearity upon straining, during the first few cycles. The ensuing

stress at zero strain occurs after the first cycle, especially at the higher strain rate coefficient. After a few cycles, the hysteresis

loop width becomes quite narrow (albeit

plasticity model for the same TGO growth rate where $\dot{\epsilon}_{growth} = 0.1\% / cycle$. Moreover, da/dN increases slightly as the creep coefficient for the substrate increases.

Layer Properties and Implications for SPLCF Life

The finite element model has been employed to study the role of the properties of the layers within the system and their influence on the rate of damage development. Each of the stages has been addressed separately. High temperature bond coat, IDZ, superalloy substrate and TGO growth strains are varied over bounds that might reasonably be expected in future systems and implications for system design discussed.

Fig. 19 shows the influence of the bond coat and interdiffusion zone strengths on the TGO crack tip extension rate for Stage I growth for a crack depth of 20 μm and a TGO thickness of 3 μm . As the crack tip at this stage is present within

the bond coat, there is a relatively strong influence of the bond coat strength on crack extension rate, with stronger bond coats inhibiting crack growth to a greater degree. At this early stage in life, interdiffusion and substrate strengths have much less influence on the process. The crack growth rate is about 6 nm/cycle, which is similar to what is observed experimentally, Fig. 7. It is important to note that about half of the overall life is spent in Stage I, so strengthening the bond coat is likely to have a strong beneficial effect on SPLCF life. It should be noted that the crack growth rate in this early stage is complex due to the shallow depth and included angle of the initial crack. As the stresses in the oxide relax, there is an uplift at the surface, as well as extension of the oxide into the material toward the interdiffusion zone; the uplift has been included in the crack length in Fig. 19, so that trends with bond coat strength are more readily apparent.

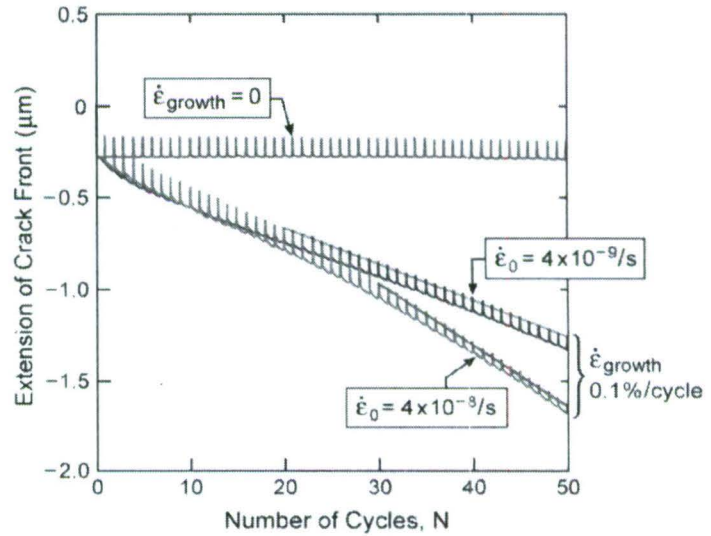


Figure 17- The crack growth rates predicted in stage III upon using the creep version of the model.

The crack tip extension rate in Stage II (crack tip in IDZ) is shown in Fig. 20. A weak interdiffusion zone will clearly accelerate the rate of damage growth, particularly if the bond coat is weak (in this case with a strength less than approximately 60 – 70 MPa). Even though the crack tip has progressed beyond the bond coat layer, the bond coat strength still influences the lengthening, since roughly half of the length of the oxide on the crack face is located along the bond coat layer. As both the bond coat and IDZ strengths approach that of the superalloy substrate, the TGO

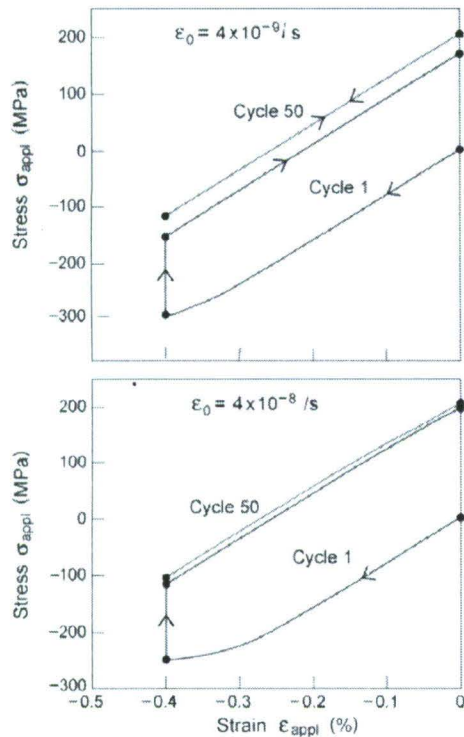


Figure 18- The evolution of stress/strain loops predicted using the creep version of the fatigue model for two values of the creep rate coefficient for the superalloy.

extension rate is minimized. However, it is important to recall that bond coat and IDZ growth strains are different from the superalloy and higher growth strains and thicker oxides (more rapid oxidation kinetics) in the substrate could drive faster crack growth. Note in Fig. 21, that the crack grows slowly in Stage II without the presence of the fatigue cycle, which is particularly detrimental for the soft bond coat. Also, as oxidation kinetics increase (the thickness of the TGO increases), the rate of damage growth increases. As Stage III is entered, the TGO extension rate is strongly influenced by the applied strain in the fatigue cycle, Fig. 22, with crack extension rates increasing by more than a factor of 10 as the applied compressive strain rises from 0.2% to 0.8%.

As the crack progresses just beyond the IDZ, there is still an influence of the bond coat and interdiffusion zone properties, again because a substantial portion of the crack face is still located within these layers. There is a complex change in rates as the cracks extend from soft layers to harder layers and the reverse, Fig 23. Nevertheless, damage growth rates all converge to a common value as the crack progresses to a depth that is 2.5 – 3X greater than the combined thickness of the bond coat and interdiffusion zone, Fig. 23. In this case, this depth is equivalent to 0.3mm, which in many airfoil designs is equivalent to the entire wall thickness [21]. This suggests that the mechanical and environmental properties of the coating and IDZ may have an unexpectedly strong effect on airfoil life.

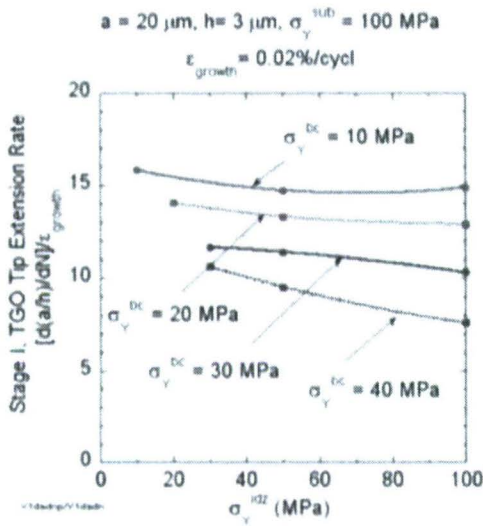


Figure 19-Influence of bond coat and IDZ on Stage I crack extension rate.

surrounding the crack tip during Stage III. As shown in Fig. 25, if this layer has a strength of less than 30 MPa and also has high growth strains, the rate of crack growth can be increased by about a factor of 5. At the present, there has been no experimental characterization of these zones, but the present results suggest that they would generally be detrimental to airfoil life.

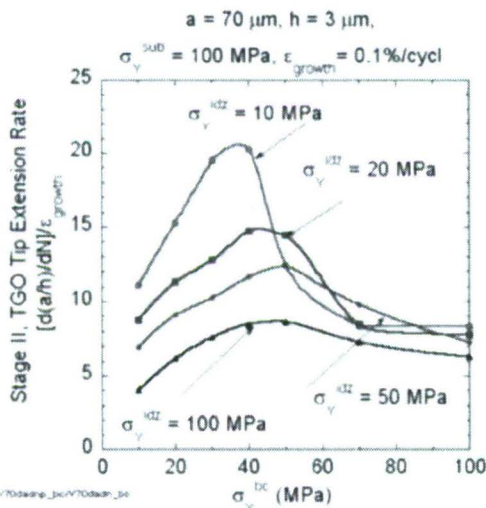


Figure 20 -Influence of bond coat and IDZ on Stage II crack extension rate.

The NiCoCrAlY bond coat material was found to undergo significant

As the crack progresses deeper into the substrate, the rate of damage growth ultimately depends on the difference in strength of the TGO compared to the substrate and the bond coat and IDZ properties become less important, Fig. 24. However, it should be recalled that only a small fraction of life is spent in these later “long crack” growth stages, Fig. 7.

To examine the role of substrate thermochemical properties and the tendency for the oxide to deplete the material of strengthening precipitates, finite element meshes were constructed to evaluate the role of soft layers of varying thicknesses

The experimental and modeling observations reported here motivate some future activities in the program, which will focus on strong bond coats with minimal interdiffusion zones. One bond coat with these characteristics has recently been developed by NIMS (National Institute for Materials Science) in Japan. This coating is referred to as the “EQ” bond coat, since it is in near-equilibrium with the superalloy substrate [22, 23]. We have recently conducted a comparative study on the oxidation behavior of the EQ coating in comparison to NiCoCrAlY coatings in furnace cycle testing (with

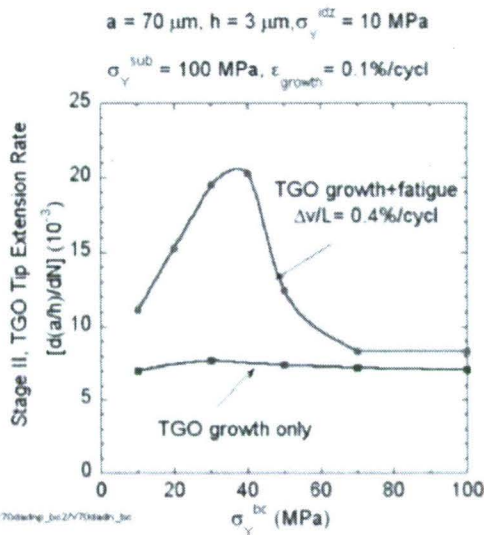


Figure 21-Role of fatigue cycling in crack growth.

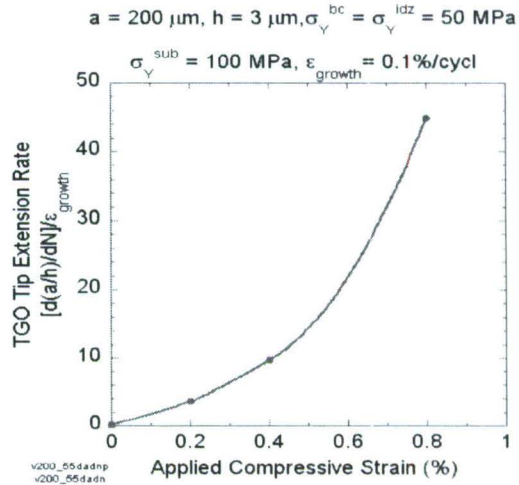


Figure 22-Acceleration of crack growth rate with applied compressive strains in the fatigue cycle.

rumpling during stepwise cycling, while the EQ coating was resistant to rumpling. If the coating is resistant to rumpling due to a higher intrinsic strength (rather than thermal expansion match with the substrate), the modeling described above suggests that this coating should also perform well in SPLCF cycling. Samples with EQ coatings for SPLCF testing are currently being processed by NIMS

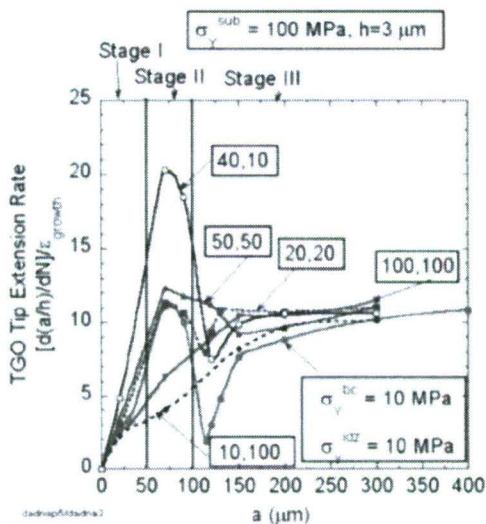


Figure 23-Crack growth rates converge to a common rate after penetrating 250 - 300 micrometers into the substrate.

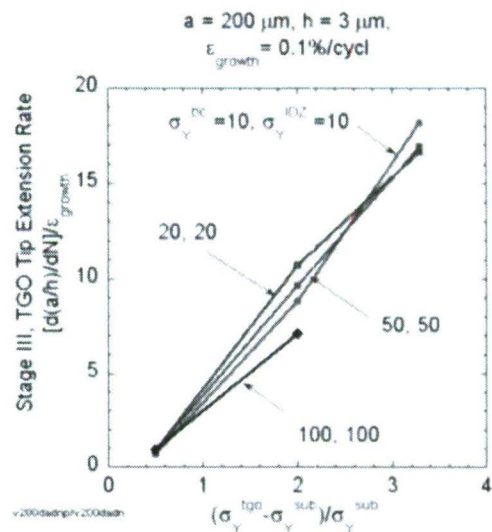


Figure 24-Stage III growth and the linear dependence on the strength differential between the TGO and substrate.

in collaboration with this program. Additionally, to further validate the modeling, samples without coatings are currently being subjected to SPLCF cycling. Modeling activities are focusing on thin-walled structures and as well as on defining coating parameters that may be measured following cycling in order to infer bond coat and IDZ properties.

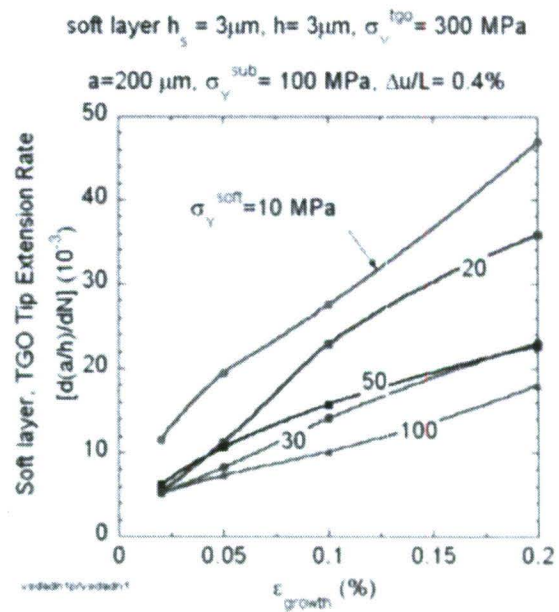
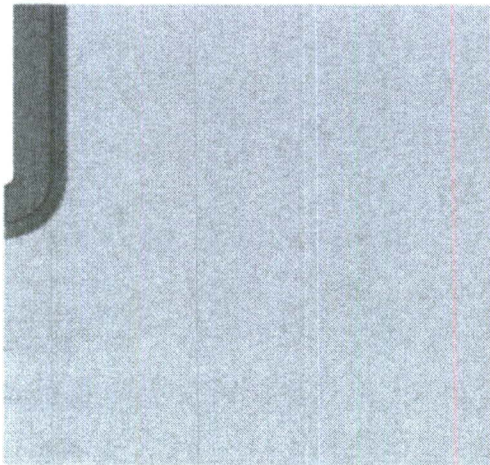


Figure 25-Schematic of the finite element model for evaluation of the properties of a soft layer (green) surrounding the TGO (red) in the crack tip (left) and the dependence of Stage III growth growth rates on the strength of the soft layer (right).

Students and Postdocs Supported

Dr. Clinique Brundidge (Current Employer: Bettis Atomic Power Laboratories)

Dr. Britta Laux (Current Employer: MTU AeroEngines)

Dr. Ming He (Current Employer: UCSB)

Papers Published

C. Mercer, K. Kawagishi, T. Tomimatsu, D. Hovis and T. M. Pollock, "A Comparative Investigation of Oxide Formation on EQ (Equilibrium) and NiCoCrAlY Bond Coats under Stepped Thermal Cycling", *Surface and Coatings Technology*, **205**, 3066 – 3072, (2011).

T.M. Pollock, B. Laux, C.L. Brundidge, A. Suzuki and M. He, "Oxide Assisted Degradation of Ni-Base Single Crystals during Cyclic Loading: The Role of Coatings", *Journal of the American Ceramic Society*, **94**, S136 – S145, (2011).

A. Suzuki, M.F.X. Gigliotti, B.T. Hazel, D.G. Konitzer and T.M. Pollock, "Crack Progression during Sustained Peak Low Cycle Fatigue in René N5, *Metall. Mater. Trans.* **41A**, 948 – 956, (2010).

M.Y. He and A.G. Evans, "A Model for Oxidation-Assisted Low Cycle Fatigue of Superalloys", *Acta Mater.* **58**, 583 – 591, (2010).

A.G. Evans, M.Y. He, A. Suzuki, M. Gigliotti, B. Hazel and T.M. Pollock, "The Mechanism Governing Sustained Peak Low Cycle Fatigue of Coated Superalloys", *Acta Materialia*, **57**, 2969 – 2983, (2009).

References

1. A. Suzuki, M.F.X. Gigliotti, B.T. Hazel, D.G. Konitzer and T.M. Pollock, "Crack Progression during Sustained Peak Low Cycle Fatigue in René N5, *Metall. Mater. Trans.* **41A**, 948 – 956, (2010).
2. J.A. Nychka, D.R. Clarke, *Oxidation of Metals*, **63**(5-6): p. 325-352 (2005).
3. V.K. Tolpygo, D.R. Clarke, *Mater. High Temp.*, **20** 261-271 (2003).
4. V.K. Tolpygo, D.R. Clarke, *Surf and Coatings Tech.*, **146 – 147**, 124-131 (2001).
5. D.S. Balint, J.W. Hutchinson, *J. Mech. Phys. Solids*, **53**, 949 (2005).
6. A. W. Davis, A. G. Evans, *Oxidation of Metals*, 1573-4889 (2006).
7. A.M. Karlsson, J.W. Hutchinson, A.G. Evans: *J. Mech. Phys. Solids*, **50**, 1565 (2002).
8. A.H. Heuer, A. Reddy, D.B. Hovis, B. Veal, A. Paulikas, A. Vlad, M. Rühle, *Scripta Materialia* **54** 1907–1912 (2006).
9. N. Birks, G.H Meier, F. S. Pettit, High temperature oxidation of metals, Cambridge University Press (2006).
10. H.J. Frost, M.F. Ashby, Deformation mechanism maps, Pergamon Press, New York, (1982).
11. A.J. Elliott, S. Tin, W.T. King, S.-C. Huang, M.F.X. Gigliotti and T.M. Pollock, "Directional Solidification of Large Superalloy Castings with Radiation and Liquid Metal Cooling: A Comparative Assessment", *Metallurgical and Materials Transactions A*, 3221 - 3231, (2004).
12. A.J. Elliott and T.M. Pollock, "Thermal Analysis of the Bridgman and Liquid-Metal Cooled Directional Solidification Investment Casting Process", *Metallurgical and Materials Transactions A*, 87-882 (2007).

13. T.M. Pollock and R.D. Field, "Dislocations and High Temperature Plastic Deformation of Superalloy Single Crystals", *Dislocations in Solids*, Vol 11, F. R. N. Nabarro and M.S. Duesbery, editors, Elsevier, Amsterdam, (2002).
14. B. W. Veal, A. P. Paulikas and P. Y. Hou, *Applied Physics Letters*, **90**, 121914 (2007).
15. A. W. Davis, A. G. Evans, *Oxidation of Metals*, 1573-4889 (2006)
16. J.S. Van Sluytman, A. Suzuki, R. Helmik, A. Bolcavage and T.M. Pollock, *Superalloys 2008*, TMS, Warrendale, PA, 499, (2008).
17. D. Pan, M.W. Chen, P.K. Wright and K.J. Hemker, *Acta Materialia* 51, 2205 – 2217, (2003).
18. I.W. Goodall, F.A. Leckie, A.R.S. Ponter and C.H.A. Townley, *Jnl Eng Mat Tech*, **101**, 349-355 (1979).
19. D.W. MacLachlan and D.M. Knowles, *Fatigue Fract Engng Mater Struct*, **24**, 503 - 521, (2001).
20. J. Telesman and L.J. Ghosn, *Eng Frac Mech*, 34 No 5/6, 1183 - 1196, (1989).
21. Y. Bihan, P.-Y. Joubert and D. Placko, *NDT&E Intl*. **34**, 363 – 368, (2001).
22. International patent pending, WO2006/104138 (published).
23. A. Sato, H. Harada, K. Kawagishi, *Metal. Mater. Trans.* **37A**, 790, (2006).